RAPID COMMUNICATIONS

PHYSICAL REVIEW B **96**, 140403(R) (2017)

Thermally driven topology in chiral magnets

Wen-Tao Hou,[1,2] Jie-Xiang Yu,[2] Morgan Daly,[2] and Jiadong Zang[2,*]
[1]*Department of Physics, Boston College, Chestnut Hill, Massachusetts 02467, USA*
[2]*Department of Physics, University of New Hampshire, Durham, New Hampshire 03824, USA*

(Received 19 May 2017; published 10 October 2017)

Chiral magnets give rise to the antisymmetric Dzyaloshinskii-Moriya interaction, which induces topological nontrivial textures such as magnetic skyrmions. The topology is characterized by integer values of the topological charge. In this work, we performed the Monte Carlo calculation of a two-dimensional model of the chiral magnet. A surprising upturn of the topological charge is identified at high fields and high temperatures. This upturn is closely related to thermal fluctuations at the atomic scale, and is explained by a simple physical picture based on triangulation of the lattice. This emergent topology is also explained by a field-theoretic analysis using CP^1 formalism.

DOI: 10.1103/PhysRevB.96.140403

The marriage of topology and condensed-matter physics has given birth to numerous excitements in the past decades. In particular, magnetism, the zoo of topological spin textures, such as domain walls, vortices and Bloch points, not only gives rise to rich physics, but also leads to transformative spintronics applications. The recently discovered magnetic skyrmion is a member of such topological textures [1–4]. It is a two-dimensional (2D) whirlpool-like structure with spins therein pointing to all directions. It has one-to-one correspondence to the three-dimensional monopole defect by stereographic mapping. The topology of the skyrmion can be captured by the topological charge (TC) [5,6],

$$Q = \frac{1}{4\pi}\int d^2r\,\mathbf{n}\cdot(\partial_x\mathbf{n}\times\partial_y\mathbf{n}), \tag{1}$$

where $\mathbf{n}$ is a unit vector describing the local spin direction. It is valued ±1 for each skyrmion, and cannot be altered by slight deformation of the texture configuration. As a result of this nontrivial topology, the skyrmion acquires interesting properties, such as the topological Hall effect and the skyrmion Hall effect [7–11], which have potential in future topological devices [12].

The magnetic skyrmion was originally proposed theoretically in noncentrosymmetric magnets [1,13–15] and its crystal form was recently discovered in bulk sample of MnSi, a typical family of noncentrosymmetric magnets, by small-angle neutron scattering [2]. It was later confirmed in (FeCo)Si thin film by real-space imaging with Lorentz transmission electron microscopy [3]. The skyrmion crystal phase in the thin film is greatly extended in the B-T diagram (where B is magnetic field and T is temperature) compared to the bulk sample, which has been further addressed by follow-up experiments [4]. This is because of the suppression of the conical phase in thin films. But nevertheless, skyrmions still exist only below the Curie temperature.

In the skyrmion crystal phase, the TC is significant and essentially counts the number of skyrmions therein. But TC in Eq. (1) respects the rotational symmetry, so that it cannot serve as an order parameter, and does not have correspondence to the crystal phase. It is interesting to study the distribution of TC in the same B-T phase diagram. To this end, we used the Monte Carlo method in this work and studied the distribution of the TC. It is significantly extended compared to the skyrmion crystal phase, and can be explained by CP^1 modeling [16,17].

We studied a 2D film of chiral magnet, whose Hamiltonian is described by the following classical spin model:

$$H = \sum_{\langle i,j\rangle}(-J\mathbf{S}_i\cdot\mathbf{S}_j + \mathbf{D}_{ij}\cdot\mathbf{S}_i\times\mathbf{S}_j) - g\mu_B H'\sum_i S_i^z, \tag{2}$$

where $\mathbf{S}_i = S\mathbf{n}_i$ is the spin on site i with $\mathbf{n}_i$, a three-dimensional unit vector, and $\langle i,j\rangle$ means the nearest neighbors. In the Monte Carlo calculation, $S = 1$ and a square lattice is employed. $J > 0$ is the ferromagnetic Heisenberg exchange coupling, while $\mathbf{D}_{ij}$ is the vector of the DM interaction between neighboring sites i and j. The strength of Dzyaloshinskii-Moriya (DM) interaction is $D = |\mathbf{D}_{ij}|$. The last term describes the Zeeman coupling, where μ_B is the magnetic moment and H' is the applied magnetic field along the z direction. We define $B = g\mu_B H'$ and choose the natural units ($\hbar = k_B = c = 1$). It has been confirmed that this simple Hamiltonian captures most essential physics of 2D chiral magnets [3,16,18].

To calculate the thermal average of the TC, we triangulated the square lattice. Summation over all the solid angles Ω of three spins on each triangle divided by 4π gives the total TC for each spin configuration (see Fig. 1). Ω is computed by the Berg formula [19]:

$$\exp\left(\frac{i\Omega}{2}\right) = \rho^{-1}[1 + \mathbf{n}_1\cdot\mathbf{n}_2 + \mathbf{n}_2\cdot\mathbf{n}_3 + \mathbf{n}_3\cdot\mathbf{n}_1 + i\mathbf{n}_1\cdot(\mathbf{n}_2\times\mathbf{n}_3)], \tag{3}$$

where $\mathbf{n}_1$, $\mathbf{n}_2$, and $\mathbf{n}_3$ are three spins on the triangle and $\rho = [2(1+\mathbf{n}_1\cdot\mathbf{n}_2)(1+\mathbf{n}_2\cdot\mathbf{n}_3)(1+\mathbf{n}_3\cdot\mathbf{n}_1)]^{1/2}$ is the normalization factor. The Metropolis [20] and over-relaxation algorithm are employed iteratively to generate a Markov chain of spin configurations [20,21], averaging over which thermal average of the TC was derived. We imposed periodic boundary conditions and performed averages over 2.4×10^6 ensembles at each temperature. The main results of the TCs are shown in Fig. 2(a). It shows the color plot of the average TC in the B-T diagram with the fixed DM interaction as $D = 0.3J$. A dramatic upturn of the TC is addressed along a ridge in the

---

[*] Jiadong.Zang@unh.edu

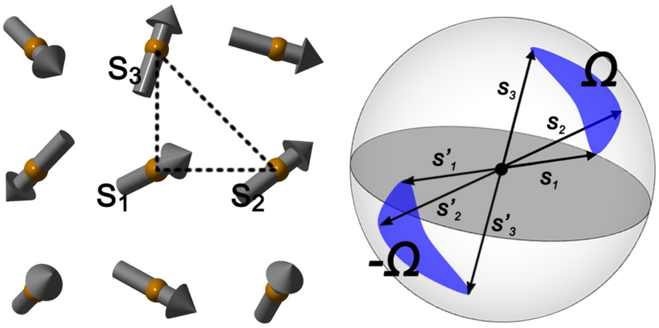

FIG. 1. Schematic diagram of the TC obtained by the solid angle Ω for each of three nearby spins $\mathbf{S}_1$, $\mathbf{S}_2$, and $\mathbf{S}_3$. This solid angle flips sign when the three spins are reversed to $\mathbf{S}_1'$, $\mathbf{S}_2'$, and $\mathbf{S}_3'$.

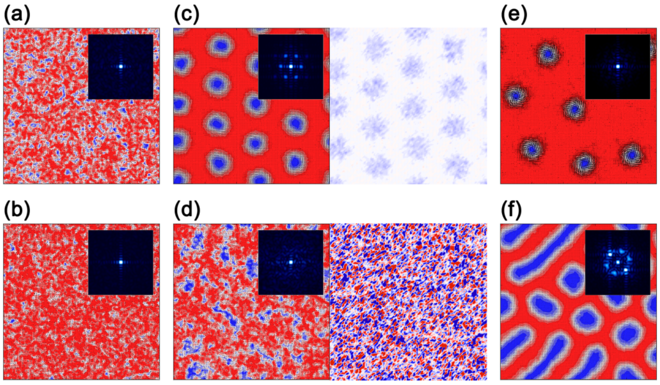

FIG. 3. Snapshots and corresponding reciprocal-space plots by fast Fourier transform (FFT) at points on the phase diagram shown in Fig. 2(a). (a) $B = 0.2J$ and $T = 1.02J$, (b) $B = 0.2J$ and $T = 0.80J$, (c) $B = 0.06J$ and $T = 0.02J$, (d) $B = 0.06J$ and $T = 0.66J$, (e) $B = 0.08J$ and $T = 0.02J$, and (f) $B = 0.02J$ and $T = 0.02J$. In real-space snapshots, red (blue) contour represent the positive (negative) value of S_{iz} and the arrows represent the directions of in-plane component. For (c) and (d), the density of TC is also shown at right panel respectively.

phase diagram. The value of the TC is significant in areas greatly extended to the skyrmion phase, which is located at small B and low T in the bottom region of the ridge.

Special attentions are paid to the high-field region, where no skyrmions are expected. As a typical example, we fix the field at $B = 0.2J$, and the relation between average TC and temperature is shown in Fig. 2(b). At very low temperature, TC is equal to zero, as all spins are nearly polarized. At very high temperature, TC again converges to zero due to the topological triviality of a completely random phase. However, in between, TC becomes significantly elevated at finite temperatures. A deep dip of the TC is witnessed around $T = 1.0J$, the Curie temperature of the corresponding Heisenberg model. Here, the negative TC is consistent with the fact that the spin at the skyrmion core is opposite to the external magnetic field. The same calculations were performed for lattices with sizes varying from 20 × 20 to 100 × 100. No difference could be found between different lattice sizes. This immunity to the finite-size effect suggests robustness of the TC upturn, which might be related to the scaling-free atomic scale physics.

This emergent topology at finite temperatures does not correspond to any ordered phase such as the skyrmion crystal phase (SkX) or meron-helix composite. Two snapshots of spin states around the ridge were taken, as shown in Figs. 3(a) and 3(b). The location of their corresponding parameters are labeled by the same letter in the B-T phase diagram in Fig. 2. At point A to the right of the ridge, $B = 0.2J$, $T = 1.02J$, and the total TC is about -12 in a 100 × 100 lattice. However, the real-space image shown in Fig. 3(a) is completely random. Fast Fourier transformation of the image provides only one peak at Γ point in the reciprocal space. This indicates the uniform randomness and absence of any spin ordering at this point. For point B to the left, where the temperature $T = 0.8J$ is relatively lower, the corresponding real-space snapshot in Fig. 3(b) shows similar randomness with a single peak at the Γ point of the reciprocal space. Compared to point A, a higher spin polarization parallel with the field is achieved here. From zero temperature to points A or B of interest, no phase transition occurs. The emergence of TC is thus purely a consequence of the thermal fluctuation.

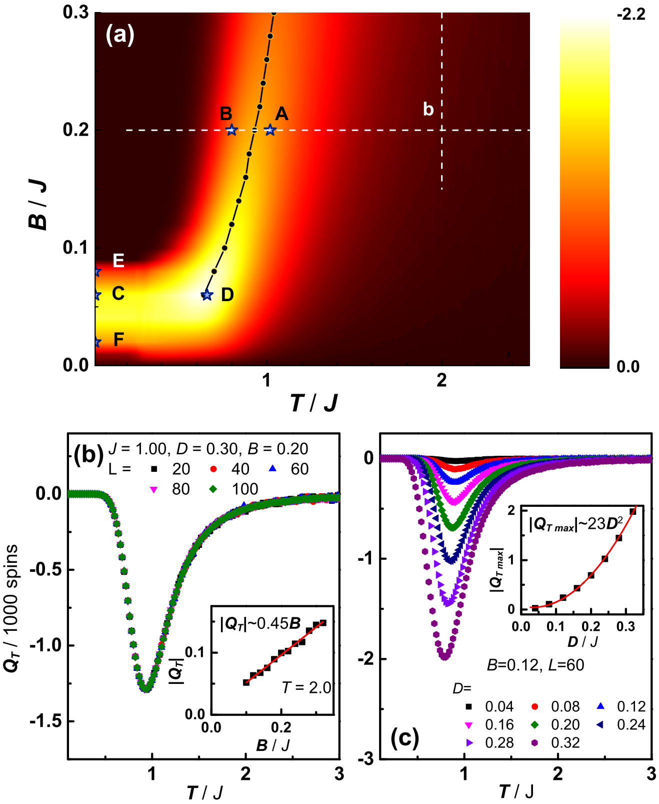

FIG. 2. Field-, temperature-, and DM-dependent TC. (a) The phase diagram of TCs with the magnetic field and temperature dependence with $D = 0.30J$. The peak value is connected as a symbolled line. The horizon and vertical dashed lines correspond to the finite size test in (b) and field-dependent TC in the inset panel of (b). Star symbols labeled A to F correspond the snapshot in Fig. 3. (c) The TC as a function of DM interaction with the fixed magnetic field $B = 0.12J$. The inset panel shows the square relationship between the peak value of TC and DM interaction.

In contrast, TCs at low field, especially at low temperatures, have distinct origin. Our Monte Carlo simulation shows that the TC grows significantly around $T = 0.25J$ during the annealing procedure and remains stable to zero temperature. It is attributed to the formation of the skyrmion crystal phase. A typical snapshot was taken at point C with $B = 0.06J$ and $T = 0.02J$ [Fig. 3(c)]. The real-space image shows a well aligned skyrmion lattice, and the reciprocal space shows the hexagonal pattern as expected. At the same field, if the temperature is elevated to point D, the snapshot in Fig. 3(d) does not present any ordering, although the TC remains significant. Densities of the TC for C and D points are plotted in Figs. 3(c) and 3(d) for comparison. Nonzero TC emerges only near the skyrmion in the ordered skyrmion phase, while it is evenly distributed in the high-temperature state. At a relatively higher field at point E [Fig. 3(e)], the skyrmion crystal is melted and sparse skyrmions are observed. While at a lower field at point F, the transition from skyrmion crystal phase to the helical phase takes place, and a meron-helix composite appears at this first-order phase transition. In all these regions at low temperatures, the TC is consistent with the number of skyrmions in the lattice. Thermal fluctuation induced TC is suppressed. These low-field low-temperature results are consistent with previous studies [8,22].

As indicated by its scaling-free property, the origin of the thermal driven topology can be understood by a simple physical picture on the atomic scale. As defined earlier, TC is the summation of solid angles of all triangles in the lattice. Due to the presence of the DM interaction, these three spins in each triangle are canted, as shown in Fig. 1, and contribute a solid angle of Ω. If we reverse all three spins, the new configuration cants an opposite solid angle Ω. In the absence of the field, these two configurations share the same energy, as both the Heisenberg and DM interactions are quadratic spin interactions. These two configurations thus have the same probability of appearance at any temperature, and the average TC is zero. However, these two configurations, being time reversed to each other, share opposite magnetizations. An external magnetic field can thus lift the degeneracy and induce a net TC after thermal averaging. One needs to be aware that under a large enough field, canting of spin takes place only when the temperature approaches the Curie temperature, far below which the polarized state is robust and the average TC is zero. On the other hand, at very high field, the energy difference induced by the field is no longer relevant, and average TC decays to zero as well. This well explains the behavior of TC in Fig. 2(b).

We can even convey this physical picture in a relatively quantitative way. Again, focus on a triangle in the lattice with three spins $\mathbf{S}_1$, $\mathbf{S}_2$, and $\mathbf{S}_3$ on the vertices. Notice that $\mathbf{S}_2$ and $\mathbf{S}_3$ are not a pair of nearest neighbors, so no direct exchange exists between them in our model. The energy of this triangle is thus given by

$$\begin{aligned} E = &-J(\mathbf{n}_1 \cdot \mathbf{n}_2 + \mathbf{n}_1 \cdot \mathbf{n}_3) - D(n_{1y}n_{2z} - n_{1z}n_{2y} \\ &+ n_{1z}n_{3x} - n_{1x}n_{3z}) - B(n_{1z} + n_{2z} + n_{3z}). \end{aligned} \tag{4}$$

In the small canting approximation, TC defined in Eq. (3) is simplified as $Q = \mathbf{n}_1 \cdot (\mathbf{n}_2 \times \mathbf{n}_3)$. Thermal average of TC is $\langle Q \rangle = \frac{1}{\mathcal{Z}} \int \prod_i d\mathbf{n}_i Q \exp(-\frac{E}{T})$, where $\mathcal{Z} = \int \prod_i d\mathbf{n}_i \exp(-\frac{E}{T})$ is the partition function. At the high-temperature limit, $E/T \ll 1$, we can expand the Boltzmann distribution in terms of polynomials of E/T. As a result, $\langle Q \rangle = \frac{1}{\mathcal{Z}} \int \prod_i d\mathbf{n}_i \mathbf{n_1} \cdot (\mathbf{n}_2 \times \mathbf{n}_3)(1 - \frac{E}{T} + \frac{1}{2!}(\frac{E}{T})^2 - \frac{1}{3!}(\frac{E}{T})^3 + \mathcal{O}[(\frac{E}{T})^4])$. The leading two orders of E/T vanish because one cannot pair up all $\mathbf{n}_i$ and their components into even powers. The leading nonzero term is the third-order term of E/T, where nonzero terms are listed in the Supplemental Material [23]. As a result, the average TC is proportional to $\frac{D^2 B}{T^3}$. That is reasonable because the TC respects spatial inversion symmetry but breaks the time-reversal symmetry; the former requires TC to be proportional to D squared, which is spatial inversion odd, while the latter enforces linear proportionality between TC and B, which is time reversal odd. No lower-order term could meet this symmetry requirement. This scaling is consistent with the numerical simulation. As shown in the inset of Fig. 2(b), the TC is truly proportional to the field at high temperatures. The relation between TC and temperature T is examined at various D values [Fig. 2(c)]. A scaling between peak value of TC and D is shown in the inset, and a perfect quadratic relation between them is identified. This quadratic relation is persistent all the way to high temperatures.

Up to now, our handwaving argument is based on only one triangle. A complete analysis is developed in terms of the CP^1 formalism of the spin model. In the continuum limit, the Hamiltonian is given by $H = \int d^2r[\frac{\bar{J}}{2}(\partial_i \mathbf{n})(\partial_i \mathbf{n}) - \bar{D}\mathbf{n} \cdot (\nabla \times \mathbf{n}) - \bar{B}n_z]$, where $i = x, y$ and $\bar{J} = JS^2$, $\bar{D} = \frac{DS^2}{a}$, and $\bar{B} = \frac{BS}{a^2}$ with finite value of $S = |\mathbf{S}|$ recovered. a is the lattice constant. A normalized two-component complex field $\mathbf{z}$ is introduced and let $n_\mu = \mathbf{z}^\dagger \sigma_\mu \mathbf{z} (\mu = x,y,z)$, where σ are Pauli matrices. In this representation, the Hamiltonian can be written in terms of a CP^1 doublet field given by

$$H = \int d^2r 2\bar{J}[|(\partial_i - i\alpha_i + i\kappa\sigma_i)\mathbf{z}|^2 - h\mathbf{z}^\dagger \sigma_z \mathbf{z}], \tag{5}$$

where $\kappa = \frac{\bar{D}}{2\bar{J}}$ and $h = \frac{\bar{B}}{2\bar{J}}$[16]. $\alpha_i = -\frac{i}{2}[\mathbf{z}^\dagger \partial_i \mathbf{z} - (\partial_i \mathbf{z}^\dagger)\mathbf{z}]$ is the emergent U(1) gauge field, whose total flux is nothing but the topological charge defined in Eq. (1):

$$Q = \frac{1}{4\pi} \int d^2r (\nabla \times \boldsymbol{\alpha})_z. \tag{6}$$

Due to the $\mathbf{z}$ dependence of $\boldsymbol{\alpha}$, the Hamiltonian has quartic terms of $\mathbf{z}$, so the integration over $\mathbf{z}$ cannot be performed straightforwardly in the partition function $\mathcal{Z} = \int \mathcal{D}\mathbf{z}^\dagger \mathcal{D}\mathbf{z} \exp(-H/T)$. Therefore, we rescale the field $\mathbf{z} \to \sqrt{\frac{2J}{T}}\mathbf{z}$, $\lambda \to \frac{1}{2}\frac{T}{J}\lambda$, define $f = \frac{T}{J}$, and perform the Hubbard-Stratonovich transformation [17,23], ending up with the partition function:

$$\begin{aligned} \mathcal{Z} = \int \mathcal{D}\mathbf{z}^\dagger \mathcal{D}\mathbf{z} \mathcal{D}\alpha_i \mathcal{D}\lambda \exp\Bigg\{ - \Bigg[&|(\partial_i - i\alpha_i + i\kappa\sigma_i)\mathbf{z}|^2 \\ &- h\mathbf{z}^\dagger \sigma_z \mathbf{z} + i\lambda\left(\mathbf{z}^\dagger \mathbf{z} - \frac{2}{f}\right)\Bigg]\Bigg\} \end{aligned} \tag{7}$$

in which $\mathbf{z}$ and $\boldsymbol{\alpha}$ are now two independent dynamical variables. A Lagrange multiplier field λ is introduced to enforce the normalization of $\mathbf{z}$.

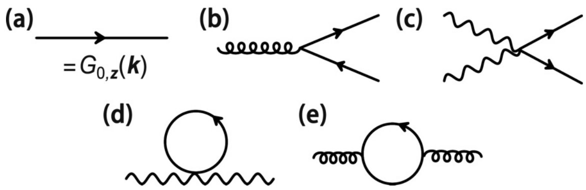

FIG. 4. Feynman rules and diagrams with various integral paths. See details in the text.

The basic idea in what follows is to integrate out the $\mathbf{z}$ field, and get an effective theory in terms of the gauge field $\boldsymbol{\alpha}$. The gauge invariance requirement gives rise to only two possible terms up to the second order of $\boldsymbol{\alpha}$ in the effective action. One is b^2 with $b = (\boldsymbol{\nabla} \times \boldsymbol{\alpha})_z$ the topological charge density, and the other is hb. A saddle-point solution of b thus gives the average value of the TC density proportional to the field h, consistent with the discussions above. To work it out, a perturbation approach is employed [24,25]. In momentum space, the unperturbed part of the action in Eq. (7) is

$$S_0 = L^2 \int \frac{d^2k}{(2\pi)^2} \mathbf{z}_k^\dagger \left(k^2 + m_0^2 - 2\kappa k_i \sigma_i\right) \mathbf{z}_k, \tag{8}$$

where L^2 is the area of the 2D film we considered. The corresponding Feynman diagram is shown in Fig. 4(a). The mass $m_0^2 = i\lambda + 2\kappa^2$ is determined by the saddle-point approximation. Denote the partition function in Eq. (7) by $\mathcal{Z} = \int \mathcal{D}\alpha_i \mathcal{D}\lambda \exp(-S_{\text{eff}}[\alpha_i,\lambda])$. A uniform saddle-point solution $i\langle\lambda\rangle = \bar{\lambda}$ and $\langle\alpha_i\rangle = 0$ solves $\delta S_{\text{eff}}/\delta\bar{\lambda} = 0$, and we finally get $\ln\frac{\Lambda^2}{m_0^2} \approx \frac{4\pi}{f}$, where $\Lambda \sim \frac{1}{a}$ is the ultraviolet cutoff in the Pauli-Villars regulation scheme [23].

The perturbative part of the action in Eq. (7) is divided into two terms,

$$S_{i1} = L^4 \int \frac{d^2kd^2q}{(2\pi)^4} \mathbf{z}_{k+q/2}^\dagger (-2k_i\alpha_{i,\,q} - 2\kappa\alpha_{i,\,q}\sigma_i - h_q\sigma_3)\mathbf{z}_{k-q/2}, \tag{9}$$

$$S_{i2} = L^6 \int \frac{d^2kd^2qd^2q}{(2\pi)^4} \mathbf{z}_k^\dagger \mathbf{z}_q \alpha_{i,p}\alpha_{i,k-q-p}. \tag{10}$$

The Feynman diagram Fig. 4(b) corresponds to S_{i1}, where the spring line represents the part $-2(k_i\alpha_{i,\,q} + \kappa\alpha_{i,\,q}\sigma_i + \frac{h}{2}\sigma_3)$ in the three-point vertex. Figure 4(c) is the four-point interaction in S_{i2}. The tilde line represents the pure emergent gauge field α_i of the four-point vertex. The first-order perturbation from S_{i2}, shown by the diagram Fig. 4(d), contributes to a term $S_d = \frac{L^4}{2\pi}\ln\frac{\Lambda^2}{m_0^2}\int\frac{d^2q}{(2\pi)^2}\alpha_i^2$. We do not consider the quadratic term of α_i at κ^2 and higher order because $\frac{\kappa^2}{\Lambda^2} \ll 1$. In contrast, the first-order perturbation of S_{i1} is a vanishing tadpole diagram. The lowest contribution is the second-order perturbation S_e depicted in Fig. 4(e). S_e can be split into two parts: S_{e1} correspond to the b^2 term and S_{e2} which includes the hb term. Combining S_d with S_{e1}, we get the gauge invariant term b^2 as expected:

$$S_{b^2} = S_d + S_{e1} = \frac{L^4}{\pi}\int\frac{d^2q}{(2\pi)^2} b_{-q}\left[\frac{\exp\left(\frac{4\pi}{f}\right)}{12\Lambda^2} + \mathcal{O}(q^2)\right] b_q. \tag{11}$$

The expected hb term also arises from the second-order perturbation. The leading term of hb in S_{e2} is

$$S_{hb} = L^4 \int \frac{d^2kd^2q}{(2\pi)^4} \frac{8\kappa^2\left(\frac{q^2}{4} + m_0^2\right)h_{-q}b_q}{\left[\left(k+\frac{q}{2}\right)^2 + m_0^2\right]^2\left[\left(k-\frac{q}{2}\right)^2 + m_0^2\right]^2} \tag{12}$$

and the effective action is therefore $S_{\text{eff}} = S_{b^2} + S_{hb}$. Solving the saddle point of the field b, we obtain

$$\bar{b} = -\frac{12\kappa^2 h}{\Lambda^2}\sinh^2\left(\frac{2\pi}{f}\right)\left[1 - \exp\left(-\frac{12\pi}{f}\right)\right]. \tag{13}$$

The thermal average of the TC at the high-temperature limit is

$$\langle Q\rangle \approx -\frac{18\pi^2 L^2 B S^5}{T^3}\left(\frac{D}{a}\right)^2\left[1 - \frac{6\pi J S^2}{T} + \mathcal{O}\left(\frac{1}{T^2}\right)\right], \tag{14}$$

where $\frac{D}{a}$ is the DM interaction in the continuum limit. This result matches well with the simple argument based on one triangle. Actually, if we further proceed to the fourth order of E/T in the single triangle argument, a term proportional to JD^2B/T^4 is present, but its sign is opposite to the $1/T^3$ term. The emergent topology at finite temperature can be thus well explained by this effective theory of the emergent gauge field.

In conclusion, we have discovered thermal driven topology in 2D chiral magnets. A significant upturn of TC was observed outside the skyrmion crystal phase. This phenomenon is well understood by both analyzing thermal fluctuations in the atomic scales and a field-theoretical approach based on CP^1 formalism. As has been extensively studied in skyrmion physics, nonzero TC would lead to the topological Hall effect, which was observed in the skyrmion crystal phase only [7,26,27]. The discrepancy between the topological Hall signal and distribution of the TC observed in this work is due to the itinerant nature of the magnetism in most chiral magnets under investigation. Close to or above the Curie temperature, the local magnetic moment in these magnets is significantly reduced so that our simulation based on constant local magnetic moment does not apply. Only in insulating magnets such as Cu_2OSeO_3 [28], local magnetic moments are persistent at elevated temperatures, and our discovery would apply. On the other hand, the thermal Hall effect related to the magnon deflection by TC has been addressed in frustrated magnets [29–31] and chiral magnets [32,33]. We therefore predict the thermal Hall effect of insulating chiral magnets, in which local magnetic moments are persistent at high fields and temperatures. Actually the phenomenon of thermal driven topology can be even generalized to ferroelectrics [34], and we would expect rich experimental observations to come out in the future.

Upon finishing this work, we noticed that similar behavior of the topological charge was recently studied by L. Rózsa *et al.* [35] and M. Randeria. Both of them studied the skyrmion crystal phase rather than the high-field case we are emphasizing in this work. We also noticed a recent work [36] which addressed a similar phenomenon in terms of skyrmion-antiskyrmion formations.

We acknowledge initial discussions with J. H. Han, O. Tchernyshyov, and D. Xiao. This work was supported by the U.S. Department of Energy (DOE), Office of Science, Basic Energy Sciences (BES) under Award No. DE-SC0016424.

[1] A. Bogdanov and A. Hubert, J. Magn. Magn. Mater. **138**, 255 (1994).
[2] S. Mühlbauer, B. Binz, F. Jonietz, C. Pfleiderer, A. Rosch, A. Neubauer, R. Georgii, and P. Böni, Science **323**, 915 (2009).
[3] X. Z. Yu, Y. Onose, N. Kanazawa, J. H. Park, J. H. Han, Y. Matsui, N. Nagaosa, and Y. Tokura, Nature (London) **465**, 901 (2010).
[4] X. Z. Yu, N. Kanazawa, Y. Onose, K. Kimoto, W. Z. Zhang, S. Ishiwata, Y. Matsui, and Y. Tokura, Nat. Mater. **10**, 106 (2011).
[5] R. Rajaraman, *Solitons and Instantons* (North-Holland, Amsterdam, 1987).
[6] N. Nagaosa and Y. Tokura, Nat. Nanotechnol. **8**, 899 (2013).
[7] A. Neubauer, C. Pfleiderer, B. Binz, A. Rosch, R. Ritz, P. G. Niklowitz, and P. Böni, Phys. Rev. Lett. **102**, 186602 (2009).
[8] S. D. Yi, S. Onoda, N. Nagaosa, and J. H. Han, Phys. Rev. B **80**, 054416 (2009).
[9] J. Zang, M. Mostovoy, J. H. Han, and N. Nagaosa, Phys. Rev. Lett. **107**, 136804 (2011).
[10] K. Litzius, I. Lemesh, B. Krüger, P. Bassirian, L. Caretta, K. Richter, F. Büttner, K. Sato, O. A. Tretiakov, J. Förster, R. M. Reeve, M. Weigand, I. Bykova, H. Stoll, G. Schütz, G. S. D. Beach, and M. Kläui, Nat. Phys. **13**, 170 (2016).
[11] W. Jiang, X. Zhang, G. Yu, W. Zhang, X. Wang, M. B. Jungfleisch, J. E. Pearson, X. Cheng, O. Heinonen, K. L. Wang, Y. Zhou, A. Hoffmann, and S. G. E. te Velthuis, Nat. Phys. **13**, 162 (2016).
[12] A. Fert, V. Cros, and J. Sampaio, Nat. Nanotechnol. **8**, 152 (2013).
[13] A. N. Bogdanov and D. A. Yablonskii, Zh. Eksp. Teor. Fiz. **95**, 178 (1989).
[14] A. N. Bogdanov and D. A. Yablonskii, Zh. Eksp. Teor. Fiz. **96**, 253 (1989).
[15] U. K. Rößler, A. N. Bogdanov, and C. Pfleiderer, Nature (London) **442**, 797 (2006).
[16] J. H. Han, J. Zang, Z. Yang, J. H. Park, and N. Nagaosa, Phys. Rev. B **82**, 094429 (2010).
[17] A. Auerbach, *Interacting Electrons and Quantum Magnetism* (Springer-Verlag, New York, 1994).
[18] B. Dupé, C. N. Kruse, T. Dornheim, and S. Heinze, New J. Phys. **18**, 55015 (2016).
[19] B. Berg and M. Lüscher, Nucl. Phys. B **190**, 412 (1981).
[20] N. Metropolis and S. Ulam, J. Am. Stat. Assoc. **44**, 335 (1949).
[21] M. Creutz, Phys. Rev. D **36**, 515 (1987).
[22] S. Buhrandt and L. Fritz, Phys. Rev. B **88**, 195137 (2013).
[23] See Supplemental Material at http://link.aps.org/supplemental/10.1103/PhysRevB.96.140403 for details of analytical calculations.
[24] O. A. Starykh, Phys. Rev. B **50**, 16428 (1994).
[25] R. K. Kaul and S. Sachdev, Phys. Rev. B **77**, 155105, (2008).
[26] S. X. Huang and C. L. Chien, Phys. Rev. Lett. **108**, 267201 (2012).
[27] Y. Li, N. Kanazawa, X. Z. Yu, A. Tsukazaki, M. Kawasaki, M. Ichikawa, X. F. Jin, F. Kagawa, and Y. Tokura, Phys. Rev. Lett. **110**, 117202 (2013).
[28] S. Seki, X. Z. Yu, S. Ishiwata, and Y. Tokura, Science **336**, 198 (2012).
[29] Y. Onose, T. Ideue, H. Katsura, Y. Shiomi, N. Nagaosa, and Y. Tokura, Science **329**, 297 (2010).
[30] M. Hirschberger, R. Chisnell, Y. S. Lee, and N. P. Ong, Phys. Rev. Lett. **115**, 106603 (2015).
[31] H. Lee, J. H. Han, and P. A. Lee, Phys. Rev. B **91**, 125413 (2015).
[32] M. Mochizuki, X. Z. Yu, S. Seki, N. Kanazawa, W. Koshibae, J. Zang, M. Mostovoy, Y. Tokura, and N. Nagaosa, Nat. Mater. **13**, 241 (2014).
[33] J. Iwasaki, A. J. Beekman, and N. Nagaosa, Phys. Rev. B **89**, 064412 (2014).
[34] S. Prokhorenko, Y. Nahas, and L. Bellaiche, Phys. Rev. Lett. **118**, 147601 (2017).
[35] L. Rózsa, E. Simon, K. Palotás, L. Udvardi, and L. Szunyogh, Phys. Rev. B **93**, 024417 (2016).
[36] M. Böttcher, S. Heinze, J. Sinova and B. Dupé, arXiv:1707.01708.